Supplementary Information

A Microfluidic Approach to Evaluating Surface Protection from Nonspecific Antibody Adsorption

Yulia Tobolovskaya†[1], Bexi M. Bustillo-Perez†[1], Yingshan Ma[1], Nadine Löw[2], Ophélie Zeyons[2], Daniel Richards[3], and Eugenia Kumacheva*[1,4,5,6]

[1] Department of Chemistry, University of Toronto, 80 Saint George street, Toronto, Ontario, ON, Canada.

[2] BASF SE, Carl-Bosch-Straße 38, D-67056 Ludwigshafen, Germany.

[3] Department of Chemistry and Applied Biosciences. ETH Zürich, Vladimir-Prelog-Weg 1, 8049 Zürich, Switzerland.

[4] Department of Materials Science and Engineering, University of Toronto, 184 College St, Toronto, ON, M5S 3E4, Canada

[5] Department of Chemical Engineering and Applied Chemistry, University of Toronto, 200 College St, Toronto, ON, M5S 3E5, Canada

[6] Institute of Biomedical Engineering, University of Toronto, 164 College St, Toronto, ON, M5S 3G9, Canada† These authors contributed equally to this work.

* Corresponding Author: Eugenia Kumacheva, Email:[eugenia.kumacheva@utoronto.ca]

S1. Characterization of C-dots and their interactions with pAbs

The size distribution of individual C-dots was obtained from TEM image analysis of fifty nanoparticles, shown in Figure S1A. The photoluminescence (PL) properties of C-dots were evaluated using fluorescence spectrophotometry. The excitation and emission PL spectra of C-dot solutions collected at an excitation wavelength of 344 nm are shown in Figure S1B. Figure S1C presents the dependence of the maximum emission wavelength on C-dot concentration. The PL stability of C-dots (0.25 mg mL^{-1}) over one week at room temperature in histidine buffer was assessed by monitoring changes in PL intensity (Figure S1D) and the corresponding shifts in the emission wavelength (Figure S1E). Finally, Figure S1F illustrates the shift in the maximum emission wavelength as a function of the $C_{pAbs}/C_{C\text{-}dot}$ ratio, demonstrating a stable wavelength during interactions with pAbs.

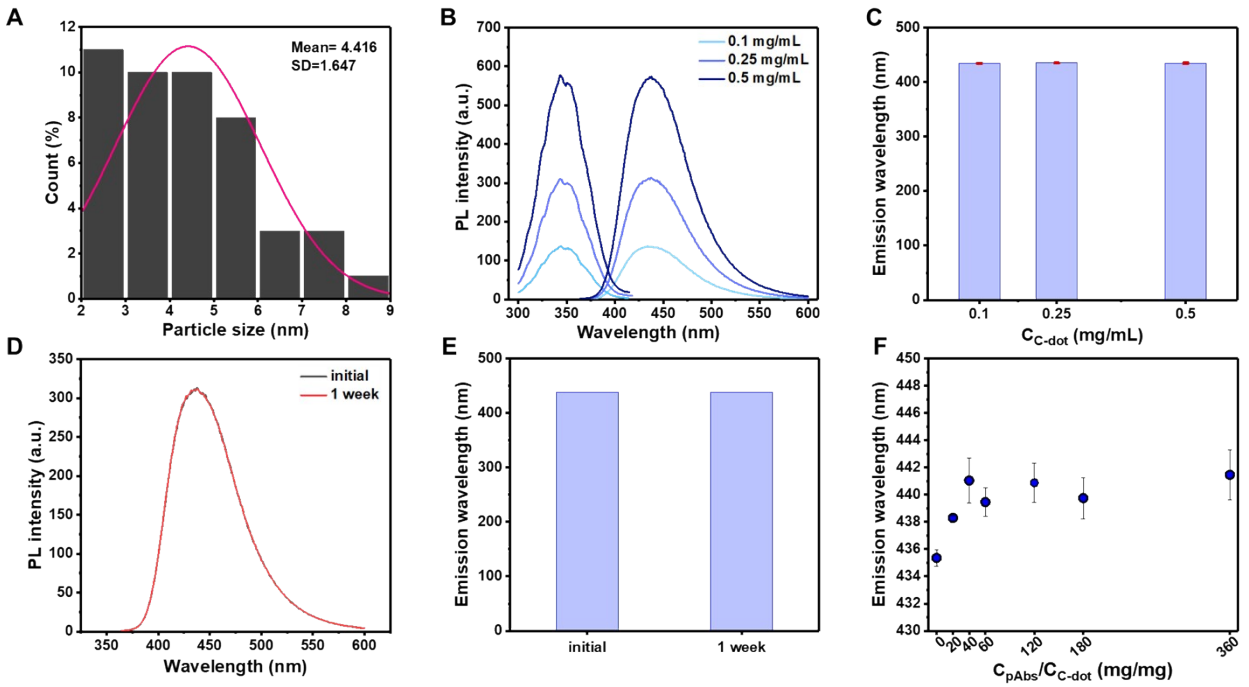

Figure S1. Characterization of C-dots and their interactions with pAbs. (A) Size distribution analysis of fifty individual C-dot nanoparticles obtained from TEM images. (B) Fluorescence excitation and emission spectra of C-dot solutions in deionized water recorded at an excitation wavelength, $\lambda_{ex,}$ of 344 nm. (C) Maximum emission wavelength of C-dots in solution of deionized water at the varying concentrations. (D) Stability of C-dots (0.25 mg mL^{-1}) in solution over one week at room temperature, showing changes in PL intensity, and (E) corresponding shifts in emission wavelength. (F) Change in the maximum emission wavelength of C-dots as a function of the $C_{pAbs}/C_{C\text{-}dot}$ ratio.

S2. Characterization of surface chemistry of C-dots

The surface chemistry of the synthesized C-dots was examined by XPS. High-resolution deconvolution of the C 1s region (Figure S2A) revealed components at 284.74, 286.15, and 288.0 eV, corresponding to C–C/C=C (23.01 at%), C–O/C–N (9.40 at%), and C=O/COOH (20.85 at%) functionalities. The N 1s spectrum (Figure S2B) exhibited peaks at 399.47 eV and 401.27 eV, assigned to N–H or pyrrolic nitrogen (15.78 at%) and graphitic or protonated nitrogen species (N–C_3 or N^+–H, 2.12 at%), respectively. The O 1s spectrum (Figure S2C) displayed contributions at 531.27 eV and 532.60 eV, associated with carbonyl (C=O, 24.16 at%) and hydroxyl (C–O, 4.31 at%) groups, confirming the presence of expected heteroatom-bearing surface functionalities on the C-dots.

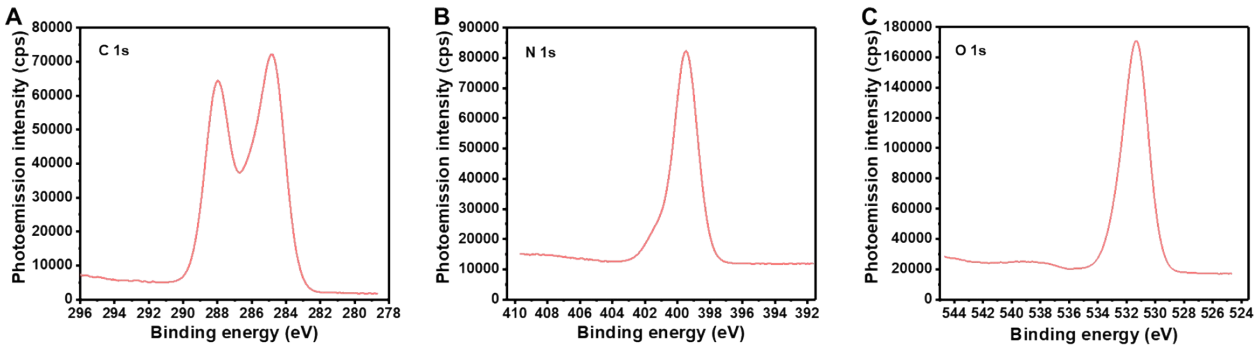

Figure S2. Characterization of surface chemistry characterization of C-dots using XPS. High-resolution XPS spectra of (A) C1s, (B) N1s, and (C) O1s core levels, demonstrating the presence of surface functional groups characteristic of the synthesized C-dots.

S3. Interactions between C-dots and proteins or polymers

The interactions of C-dots with BSA and Kolliphor® P 188 Bio were assessed using fluorescence spectrophotometry and ITC. Figure S3A presents a calibration curve of I/I_0 as a function of increasing BSA concentration, enabling comparison between the quenching contributions from pAbs (96% purity) and the estimated 4% BSA impurity present in the antibody formulation. Figures S3B and S3C show the PL emission spectra of C-dots during incubation with Kolliphor® P 188 Bio and the corresponding I/I_0 values at varying $C_{Kolliphor^{®}\ P\ 188\ Bio}/C_{C\text{-}dot}$ ratios over time, respectively, confirming absence of interactions between this polymer and our fluorescence reporter. The shift in the C-dot emission wavelength as a function of $C_{Kolliphor^{®}\ P\ 188\ Bio}/C_{C\text{-}dot}$ is shown in Figure S3D. Figures S3E and S3F display ITC thermograms acquired by titrating C-dots into Kolliphor P188 Bio at $C_{Kolliphor^{®}\ P\ 188\ Bio}/C_{C\text{-}dot}$ = 35 mg mg^{-1} (below the critical micelle concentration) and 160 mg mg^{-1} (at the critical micelle concentration), respectively.

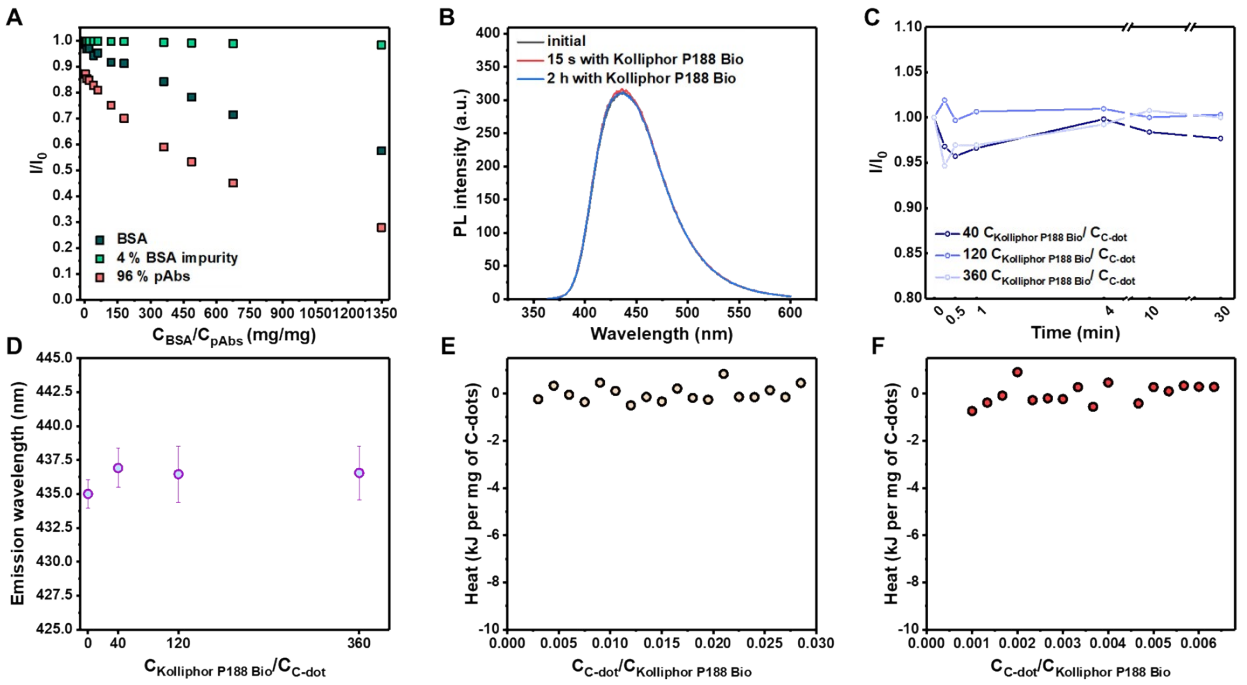

Figure S3. Interactions between C-dot fluorophores and proteins or surfactant molecules. (A) Calibration curve of I/I₀ as a function of $C_{BSA}/C_{C\text{-}dot}$, comparing the quenching contributions of pAbs (96% purity) and the estimated 4% BSA impurity in the antibody formulation. (B) Fluorescence emission spectra of C-dots during incubation with Kolliphor® P 188 Bio and (C) corresponding I/I₀ at varying $C_{Kolliphor^{®}\ P\ 188\ Bio}/C_{C\text{-}dot}$ ratios over time. (D) Shift in C-dot emission maximum as a function of $C_{Kolliphor^{®}\ P\ 188\ Bio}/C_{C\text{-}dot}$. (E) ITC profile of C-dots titrated into Kolliphor® P 188 Bio at $C_{Kolliphor^{®}\ P188\ Bio}/C_{C\text{-}dot}$ = 35 mg mg^{-1}, and (F) 160 mg mg^{-1}.

S4. Comparative XPS analysis of C-dots on APTES-modified silicon surface

The attachment of C-dots to silicon substrates was evaluated by XPS on both non-modified and APTES-functionalized wafers. Figure S4A shows the survey spectrum of the APTES-modified silicon wafer prior to C-dot deposition, displaying the expected contributions from carbon, nitrogen, oxygen, and silicon. High-resolution spectra confirmed successful formation of the APTES monolayer: the C 1s region (Figure S4B) displayed peaks consistent with the alkylsilane backbone, while the N 1s spectrum (Figure S4C) contained three components, including a dominant primary amine peak at 399.02 eV (5.16 at%), a protonated amine signal at 400.51 eV (1.2 at%), and a weak component at 401.41 eV (0.71 at%) attributed to hydrogen-bonded or partially oxidized nitrogen species. Following exposure of the APTES-modified wafer to a C-dot solution, the XPS analysis revealed clear evidence of covalent attachment. First, the survey spectrum (Figure S4D) showed a significantly lower silicon substrate signal after extensive rinsing

with water, consistent with the presence of a stable, surface-bound C-dot layer. High-resolution C 1s and N 1s spectra (Figures S4E and S4F) showed pronounced peaks at 288.16 eV (11.32 at%) and 399.86 eV (9.17 at%), corresponding to amide carbonyl and amide nitrogen species, respectively, confirming the formation of amide linkages between the C-dots and APTES. In contrast, the non-modified silicon wafer exposed to the same solution of C-dots and rinsed under identical conditions exhibited a stronger silicon substrate signal (Figure S4G), weak carbon features (Figure S4H), and a low nitrogen content (2.28 at%) (Figure S4I), indicating only physical C-dot adsorption to the substrate in the absence of APTES.

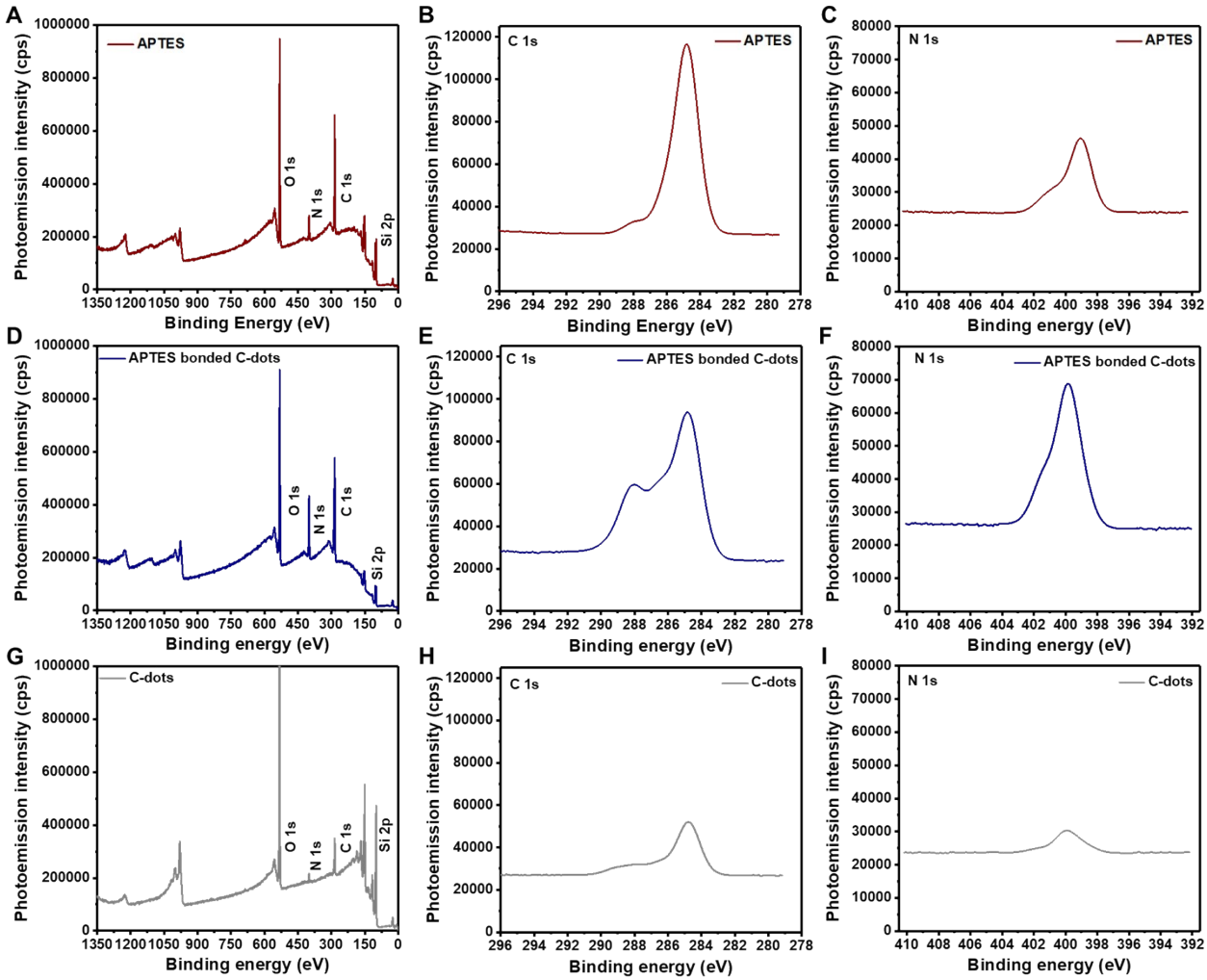

Figure S4. XPS analysis of silicon wafer modified with APTES including (A) survey spectra, (B) high-resolution C1s and (C) N1s spectra confirming formation of APTES monolayer. Comparative analysis of C-dots on APTES-modified and non-modified silicon substrates, respectively, including (D,G) survey spectra, (E,H) high-resolution C1s and (F,I) N1s spectra supporting covalent bond formation between C-dots and APTES via amide linkages.

S5. Functionalization of microchannel surface with C-dots

Figure S5A shows the change in the I/I_0 ratio when 5 µL of the histidine buffer was perfused through the microchannel in each perfusion step. After the fourth perfusion step, the value of I/I_0 did not change, indicating that C-dots were not washed away.

Figure S5B shows fluorescence microscopy images of the MF channels subjected to C-dot solutions with different $C_{C\text{-}dot}$. At $C_{C\text{-}dot}$ of 20-100 mg mL^{-1}, surface aggregation of C-dots took place, whereas at low $C_{C\text{-}dot}$ = 4.0 mg mL^{-1} only a weak fluorescence signal was observed.

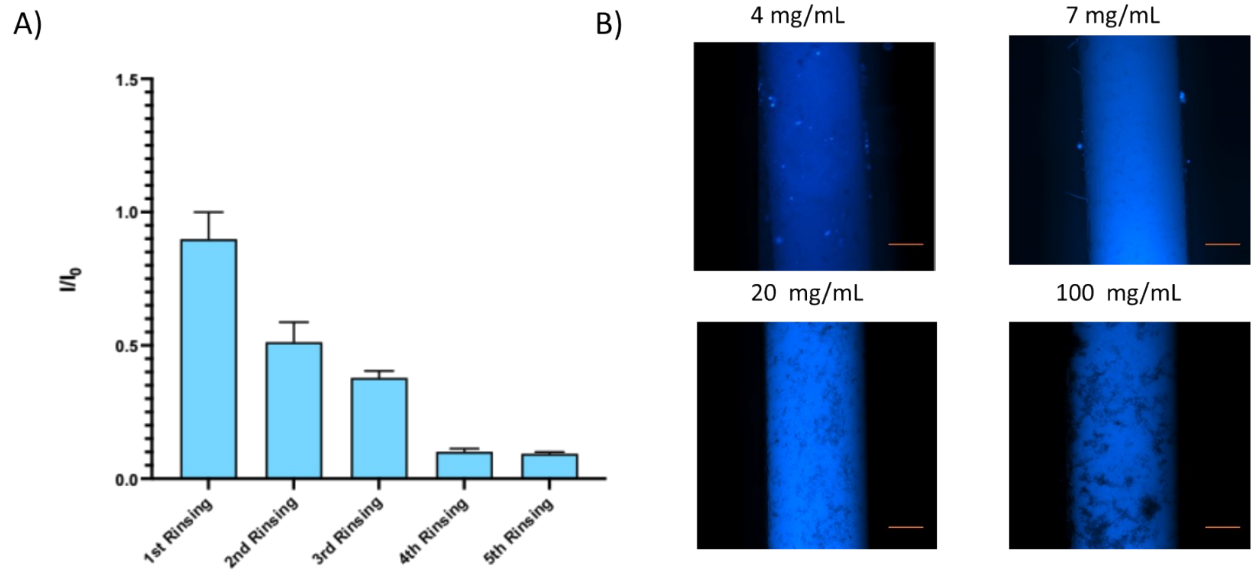

Figure S5. (A) Normalized fluorescence intensity of rinsing solutions collected from PDMS microchannels. (B) Fluorescence microscopy images corresponding to channels incubated with C-dot solutions at 4.0, 7.0, 20, and 100 mg mL^{-1} for 12 h, followed by sequential rinsing. Scale bar: 200 µm.

S6. Quantification of C-dot surface density on PDMS microchannels

After incubation of C-dot solution with a particular $C_{C\text{-}dot}$ in the microchannel, it was rinsed four times with 5 µL of deionized water. To determine the surface density of C-dots in the microchannel with a total surface area of 1.5 cm^2 (Figure S6A, and S6B), the concentration of C-dots in the supernatant and deionized water was determined using the calibration graph generated by plotting the PL intensity of C-dot solutions as a function of $C_{C\text{-}dot}$ (Figure S6C) as described in the Methodology section. In contrast to the APTES-modified channels (Figure S6A), the non-modified

PDMS channels exhibited substantially lower C-dot surface densities (Figure S6B), consistent with weak, physical adsorption in the absence of APTES.

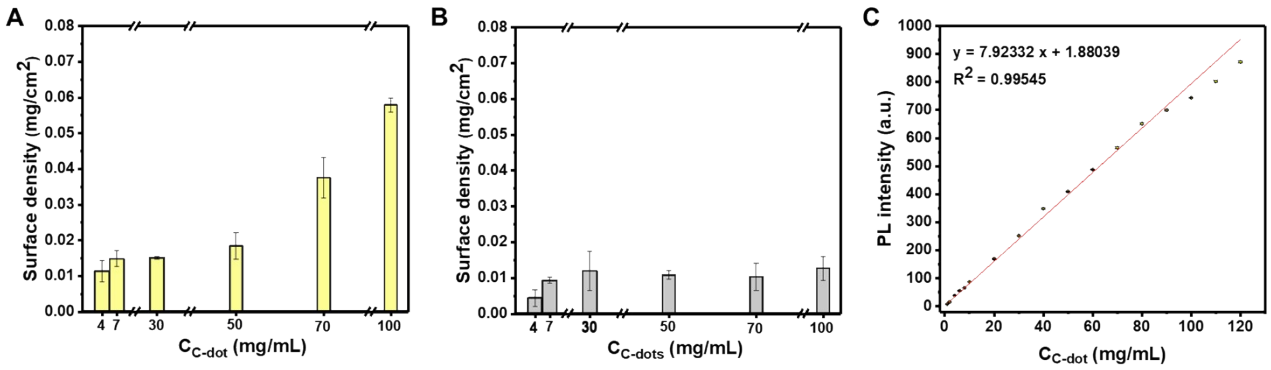

Figure S6. Quantifying the surface density of C-dots on the surface of microchannels. Surface density of C-dots on the surface of APTES-modified channels (A) and the surface of non-modified channels (B). (C) Calibration graph of the PL intensity of C-dots *vs.* $C_{C\text{-}dot}$. Error bars represent mean ± standard deviation (n = 3 independent experiments). For the 70 and 100 mg mL^{-1} condition in (A), n=2 was used.

S7. Fluorescence microscopy images of non-modified microchannels

Fluorescence microscopy was used to visualize the distribution and extent of C-dot attachment within non-modified MF channels of PDMS after incubation with varying $C_{C\text{-}dot}$ and subsequent rinsing. As shown in Figure S7, non-modified channels exhibited a weak fluorescence signal across all tested concentrations, demonstrating a limited attachment of C-dots in the absence of APTES surface functionalization.

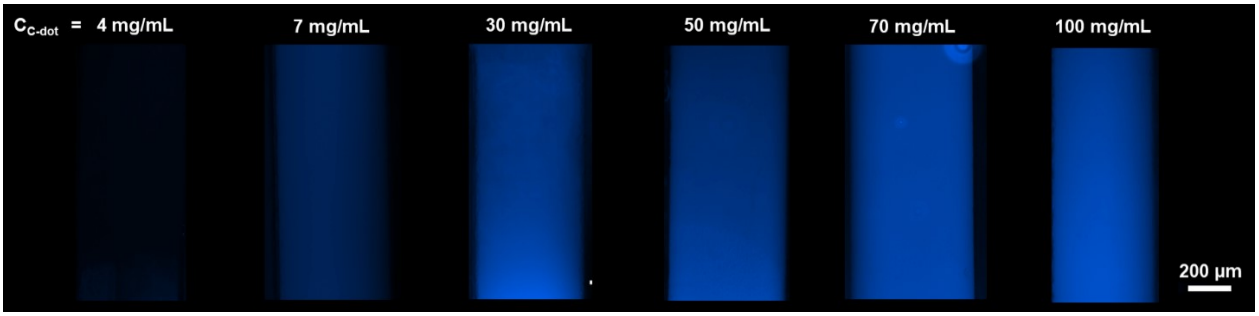

Figure S7. Fluorescence microscopy images of non-modified MF PDMS channels following incubation with C-dots at varying $C_{C\text{-}dot}$ and subsequent rinsing steps. Non-modified PDMS channels exhibiting substantially lower residual fluorescence across all conditions, demonstrating limited C-dot adsorption in the absence of APTES surface modification.

S8. Examination of pAbs adsorption to C-dot-functionalized PDMS using QCM-D

The performance of the fluorescence assay-based MF platform for quantifying antibody adsorption was compared and validated with conventional QCM-D analysis. Figure S8A shows baseline stabilization of the resonance frequency signal during perfusion of histidine buffer over unprotected PDMS sensor surfaces. Baseline stabilizations on C-dot functionalized APTES–PDMS surfaces treated with Kolliphor® P 188 Bio and Kolliphor® PS 20 are presented in Figures S8B and S8C, respectively. Figure S8D depicts the initial perfusion of histidine buffer into the C-dot modified APTES–PDMS sensor chamber, establishing a stable baseline prior to the perfusion of pAbs. Representative frequency shifts (Δf_7) during perfusion of pAbs at increasing concentrations are shown in Figure S8E, reflecting the progressive adsorption of antibodies onto the sensor surface. The calibration curve correlating adsorbed pAbs surface density (ng/cm²) with the corresponding C_{pAbs} is presented in Figure S8F, demonstrating a quantifiable adsorption behavior of pAbs onto C-dot functionalized PDMS.

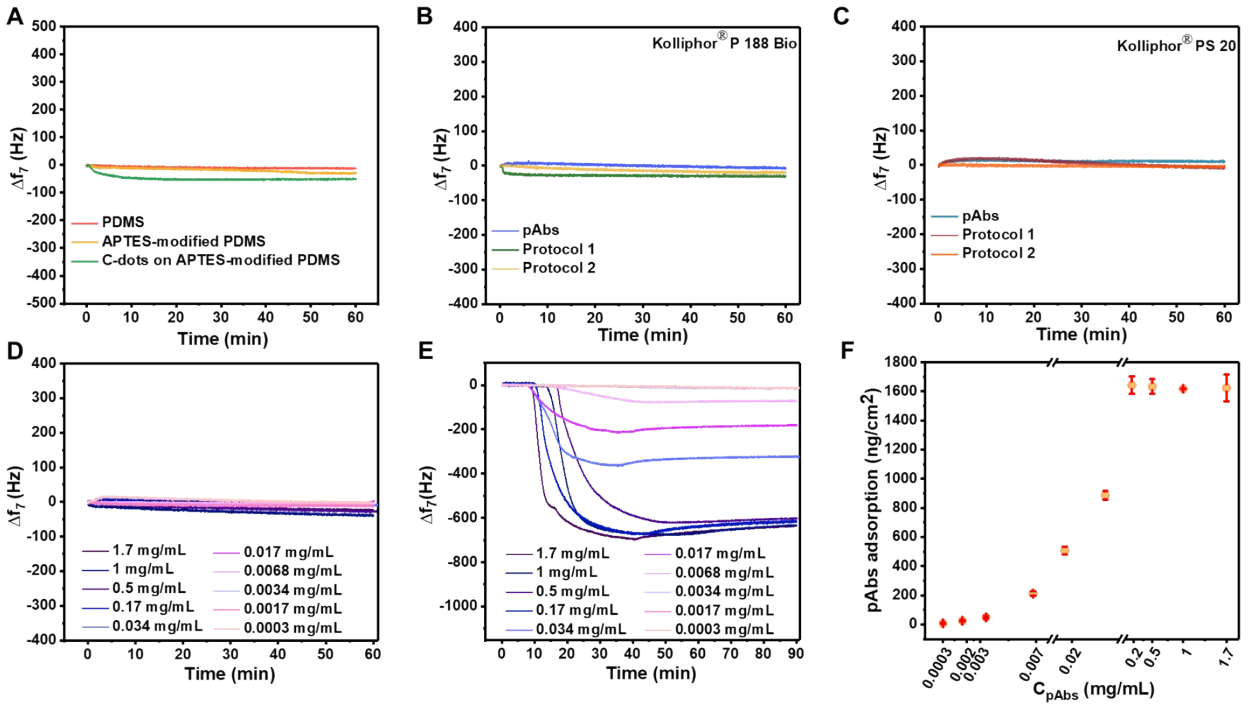

Figure S8. QCM-D-based analysis for quantifying pAbs adsorption to PDMS surfaces. (A) Baseline stabilization of the resonance frequency signal during histidine buffer perfusion over non-protected PDMS-based sensor surfaces. (B, C) Baseline stabilization during perfusion over C-dot functionalized APTES–PDMS surfaces treated with Kolliphor® P 188 Bio and Kolliphor® PS 20, respectively. (D) Initial perfusion of histidine buffer into the chamber containing the C-dot modified APTES–PDMS sensor, establishing a stable baseline prior to pAbs perfusion. (E) Representative frequency shifts (Δf_7) recorded during perfusion of pAbs at increasing

concentrations. (F) Calibration curve correlating the adsorbed pAbs surface density (ng/cm²) with the corresponding C_{pAbs}, demonstrating a measurement sensitivity of 0.00034 – 0.17 mg mL^{-1}. The reported values of mass of adsorbed pAbs per surface area represent the mean and standard deviation from three independent repeats.

S9. Accounting for pAbs autofluorescence

The pAbs used in the present work exhibited weak but measurable autofluorescence. The intrinsic autofluorescence of IgG antibodies is well-established and is ascribed primarily to the presence of aromatic amino acid residues, particularly, tryptophan, with minor contributions from tyrosine.[1-5] The impact of autofluorescence of pAbs in the present work was evaluated by using fluorescence microscopy and fluorescence spectrophotometry (Figure S9). Control experiments performed for perfusion of the pAbs solution through the APTES-modified microchannel, before its modification with C-dots, revealed a weak PL signal. In these experiments, the PL intensity increased when pAbs concentration in the solution changed from 10 to 300 mg mL^{-1} (Figure S9A). To further validate this observation, excitation and emission spectra of pAbs were recorded within the spectral range used for C-dot detection (λ_{ex} = 344 nm), as shown in Figure S9B. These results indicated partial spectral overlap between pAbs autofluorescence and PL of C-dots.

In the MF experiments, the contribution of pAbs autofluorescence to the measured variation in PL intensity of C-dots due to the quenching effect was accounted for by subtracting the PL signal of pAbs as a background. More specifically, a solution with a particular pAbs concentration was first perfused through an APTES-modified control microchannel for 5 min, and the corresponding PL intensity, I_{pAbs} was recorded. This signal was then subtracted from the total PL intensity, I_{total}, measured at time t after perfusing the pAbs solution with the same concentration through the C-dot-modified microchannel. The normalized PL signal of C-dots was calculated as

$$I/I_0 = \frac{\left(I_{total} - I_{pAbs}\right)_t}{\left(I_{total} - I_{pAbs}\right)_{t_0}}, \qquad (1)$$

where t_0 = 15 s after introducing the pAbs solution in the C-dot-modified microchannel.

All MF perfusion experiments of pAbs through C-dot-modified and control channels were performed at a flow rate of 2 µL min^{-1}. All PL intensity measurements were performed using a microscope configuration under a Nikon DAPI filter set (UV excitation, blue emission collection)

with a 4× objective, a constant exposure time of 300 ms, and a fixed 100 × 100 pixel ROI positioned at the center of the microchannel for all experiments.

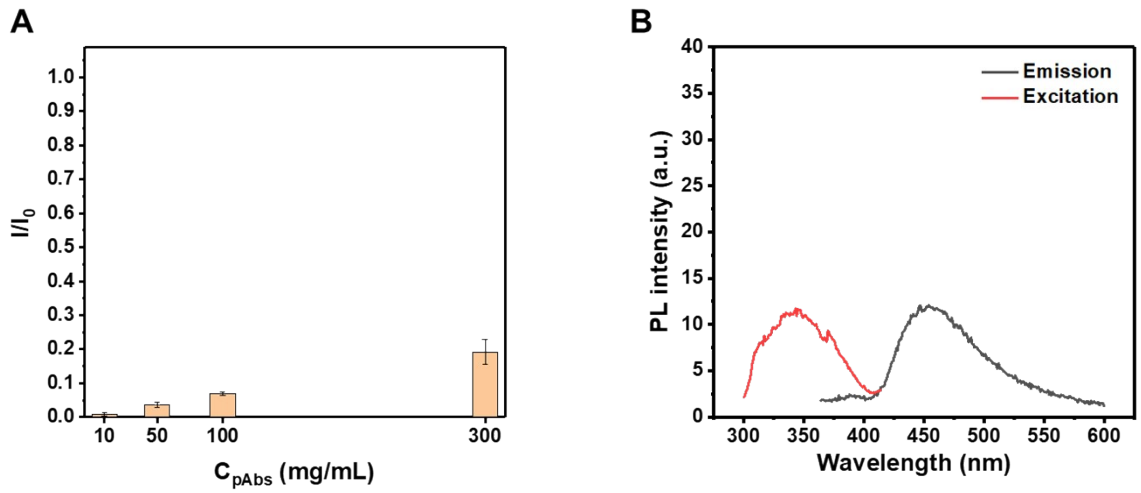

Figure S9. Characterization of pAbs autofluorescence. (A) Fluorescence intensity of the region of interest measured at 300 s during perfusion of pAbs through an APTES-modified microchannel in the absence of C-dots. The values represent the variation in normalized intensity (I/I_0) at the lowest and highest pAbs mass concentrations, where I is the PL intensity at the given time point and I_0 is the initial PL intensity of the C-dot channel, demonstrating a relatively weak intrinsic fluorescence of the antibodies compared to PL of C-dots. (B) Fluorescence spectrophotometry measurements showing the excitation and emission spectra of pAbs, recorded under the same spectral conditions used for C-dot detection.

S10. Evaluation of PL Signal Uniformity along MF Channels

Figure S10 shows the PL intensity profiles measured along C-dot–modified PDMS microchannels to assess the spatial distribution of C-dots. The microchannels which were filled with either 10, or 20 mg mL^{-1} C-dot solutions exhibited the variations in PL intensity. In contrast, channel exposure to 7 mg mL^{-1} C-dot solution resulted in uniform PL distribution, ensuring that all regions of interest would exhibit consistent PL quenching.

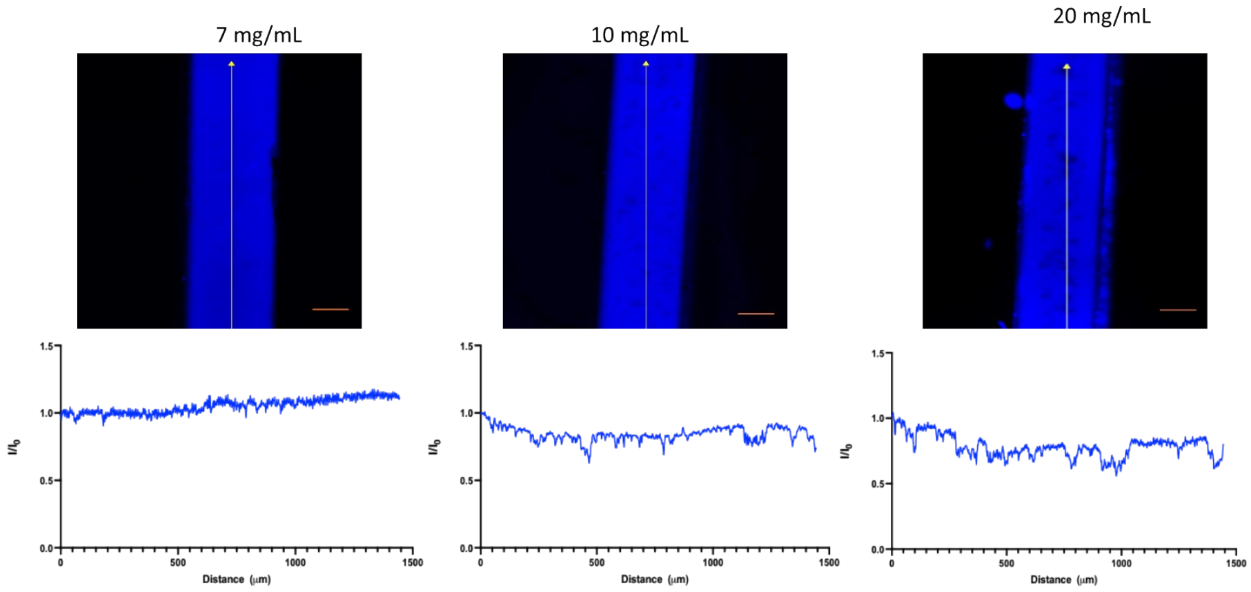

Figure S10. Photoluminescence intensity profiles measured along 1500-µm lines drawn along the channels. The profiles correspond to channels incubated with C-dot solutions of 7.0, 10, and 20 mg/mL (left to right). Scale bar is 200 µm.

S11. Bradford assay

The Bradford assay was used to determine the concentration of pAbs in histidine buffer perfused through polymer-protected microchannels. Figure S11A shows the calibration graph generated to quantify pAbs concentrations in the solutions collected in Protocol 1 or Protocol 2 experiments using either Kolliphor® P 188 Bio, or Kolliphor® PS 20. The calibration graph was constructed from the absorbance readings of a series of standard pAbs solutions ranging from 10–1500 µg/mL. To verify whether either polymer affects Bradford measurements, 0.05 wt% solution of Kolliphor® PS 20 or Kolliphor® P188 Bio was added to 48-well plates preloaded with 300 µL of Bradford reagent, incubated for 5 min, and analyzed with the plate reader. Sample wells containing only Bradford reagent served as controls for baseline correction. Figure S11B shows the results of absorbance measurements at 595 nm for Bradford reagent alone, Bradford reagent mixed with Kolliphor® PS 20, and Bradford agent mixed with Kolliphor® P 188 Bio. A stronger absorbance observed for the Kolliphor® PS 20 mixture indicates that this polymer interacts more effectively with Bradford reagent than Kolliphor® P 188 Bio. To ensure accurate determination of pAbs concentrations, the absorbance contribution from Kolliphor® PS 20 was subtracted from sample readings.

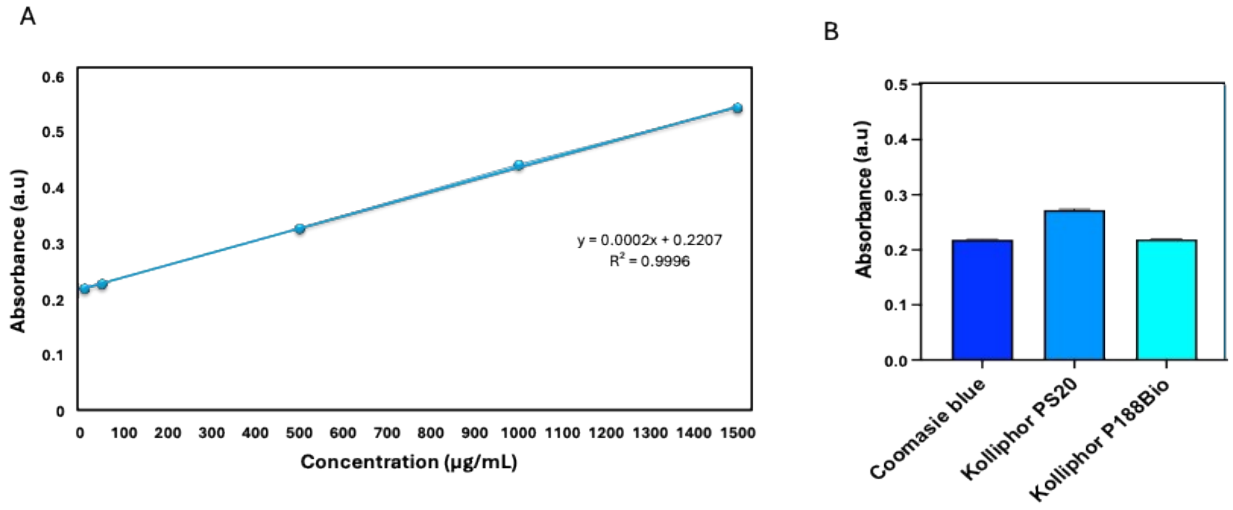

Figure S11. (A) Calibration graph generated for pAbs solutions with known concentration. (B) Absorbance of Bradford reagent alone and Bradford reagent mixed with either Kolliphor® PS 20, or Kolliphor® P 188 Bio.

References

1. Lakowicz, J. R. Introduction to Fluorescence. In Principles of Fluorescence Spectroscopy; Springer: Boston, MA, **2006**; pp 1–26.
2. Vekshin, N. L. Division of Tyrosine and Tryptophan Fluorescence Components. In Photonics of Biopolymers; Biological and Medical Physics Series; Springer: Berlin, Heidelberg, **2002**; pp 213–236.
3. Brack, L.; Merkel, O.; Schroeder, R. A Rapid Method to Monitor Structural Perturbations of High-Concentrated Therapeutic Antibody Solutions using Intrinsic Tryptophan Fluorescence Emission Spectroscopy. *Eur. J. Pharm. Biopharm.* **2024,** *201***,** 114377**.**
4. Engström, H. A.; Andersson, P. O.; Ohlson, S. A Label-Free Continuous Total-Internal-Reflection-Fluorescence-Based Immunosensor. *Anal. Biochem.*, **2006**, *357*, 159–166.
5. Gore, M. G.; Bottomley, S.; Popplewell, A. G.; Atkinson, T. The Use of Tryptophan Fluorescence to Determine the Stability of IgG Binding Proteins Based Upon the B Domain of Protein A from Staphylococcus aureus. *Biochem Soc Trans.* **1992**, *20*, 288S.